Engineered Science
DOI: https://dx.doi.org/10.30919/es1695

Microstructure and Tribological Properties of Plasma Sprayed FeCoNiCrMo and FeCoNiCrMn High-Entropy Alloy Coatings

Yi Wang,[1] Yonggang Guo,[1,*] Sri Hari Kumar Annamareddy,[2] Qing Zhang,[1] Xinchao Wang,[1] Wenhuan Zhu,[1] Zichao Guo,[1] Zhongpu Wang[1] and Xiaohang Jing[1]

Abstract

In this study, FeCoNiCrMo and FeCoNiCrMn high-entropy alloy coatings were successfully prepared on KmTBCr12 iron substrates by plasma spraying technology. The microstructure and phase composition of the coatings were analyzed, and the effects of spraying current and spraying distance on hardness, bonding strength, and porosity were systematically investigated. Additionally, the wear resistance mechanisms of the two coatings were compared. The experimental results show that both coatings exhibit a strong metallurgical interface with partially developed lamellar eutectic patterns. The critical process variables significantly impact the coating hardness, bonding strength, and porosity. Elemental distribution analysis confirms that oxide formation occurs in all metal components of the coating, which greatly improves its hardness and tribological properties. The FeCoNiCrMo coating exhibits a 2.52-fold increase in hardness compared to the substrate, which is attributed to solid-solution hardening induced by Mo additions. Under dry sliding friction conditions, the wear rates of the FeCoNiCrMo and FeCoNiCrMn coatings are reduced by 89 % and 78 %, respectively, relative to the substrate. After the coatings are applied to the substrate surface, the wear mechanism changes from adhesive wear to abrasive and fatigue wear.

Keywords: Microstructure; Tribological property; Plasma spraying; High entropy alloy coating.

Received: 21 May 2025; Revised: 30 June 2025; Accepted: 18 August 2025.
Article type: Research article.

1. Introduction

The roller mill is the primary equipment used for processing wheat into flour. Its working principle involves grinding wheat grains between two parallel and oppositely rotating grinding rollers.[1] The grinding roller is a critical component that directly impacts the operational stability, flour yield, and nutritional quality. Grinding rollers are generally categorized into toothed rollers and sandblasting rollers, which are applied in skin mill and core mill systems, respectively. However, during the grinding process, the wear on the roller surface alters its geometric properties.[2] Although numerous researchers have enhanced the wear resistance of grinding rollers through surface treatment technologies such as carburizing, nitriding, laser quenching, and physical vapor deposition,[3-6] the low hardness and insufficient wear resistance of grinding rollers continue to significantly impact the quality and processing efficiency of flour.

Coating techniques are widely applied across various industrial sectors such as aerospace engineering, nuclear power systems, petrochemical processing, automotive production, and electronic device manufacturing.[7-9] These surface modification methods effectively extend operational lifespans of critical components while expanding material selection possibilities.[10-12] A novel advancement in this field involves high configurational entropy metallic coatings,[13,14] demonstrating outstanding characteristics including exceptional mechanical strength,[15] elevated hardness,[16] superior wear resistance,[17-19] robust corrosion tolerance,[20,21] and remarkable high-temperature oxidation stability.[22] These enhanced properties originate from distinctive mechanisms: entropy maximization, crystalline lattice distortion effects, sluggish atomic diffusion kinetics, and synergistic elemental interactions.[23,24] Specifically, FeCoNiCrMo and FeCoNiCrMn alloy systems have attracted significant research interest due to their optimized mechanical

[1] *Henan Key Laboratory of Superhard Abrasives and Grinding Equipment & School of Mechanical and Electrical Engineering, Henan University of Technology, Zhengzhou, 450001, China*
[2] *Department of Chemical and Petrochemical Engineering, College of Engineering and Architecture, University of Nizwa, Nizwa, 616, Oman*
**E-mail*: nanogyg@163.com (Y. Guo)

performance coupled with exceptional tribological and anti-corrosive capabilities. Contemporary fabrication approaches incorporate advanced deposition methods such as magnetron sputtering, laser cladding, and thermal spraying techniques.[25-27] Particularly noteworthy is plasma spraying technology a high-temperature coating process utilizing ionized gas streams, which offers distinct advantages including operational efficiency, rapid layer formation rates, and broad material adaptability.[28] It is currently the most prevalent method for the thermal spraying of high-entropy alloy coatings.[29]

Extensive investigations have been performed on the microstructural characteristics and performance metrics of FeCoNiCrMo and FeCoNiCrMn high-entropy alloy surface layers. In pioneering work by Qiu and Zuo, CoCrFeNiMo coatings were successfully fabricated on medium-carbon steel substrates through laser cladding methodology. Their phase analysis identified a face-centered cubic (FCC) matrix alongside body-centered cubic (BCC) and Laves phases, achieving remarkable surface hardness values up to 741 HV.[30,31] Li *et al*. evaluated two thermal spray techniques for $FeCoCrNiMo_{0.2}$ deposition, revealing that plasma spaying specimens demonstrated enhanced tribological performance relative to high-velocity oxygen fuel counterparts, primarily attributed to oxide-induced lubrication mechanisms.[32] Subsequent studies by Wang's research group systematically examined Mo concentration effects on multifunctional properties.[33] Elevated Mo levels induced multiple strengthening mechanisms including substitutional atom reinforcement, grain refinement effects, and secondary phase precipitation.[34,35] Concurrently, competitive corrosion dynamics between subgrain boundaries improved anti-corrosion characteristics, with observed degradation processes combining mechanical abrasion, material transfer phenomena, and electrochemical dissolution.[36] Parametric optimization studies by Zhang *et al*. demonstrated that enhanced power input during spraying operations increased coating hardness while effectively suppressing crack propagation.[37] High-temperature oxidation investigations conducted by Wen *et al*. identified protective Cr_2O_3 scale formation at 1100°C under steam conditions, significantly retarding substrate oxidation in Zr-4 alloy systems.[38] Innovative composite coating development by Ren and Cui incorporated WC particulates and CeO_2 additives into $FeCoNiCrMo_{0.2}$ matrices via laser deposition, achieving substantial grain structure refinement alongside reduced defect density and improved mechanical properties.[39,40]

Recent studies on FeCoNiCrMn high-entropy alloy (HEA) coatings have demonstrated varied fabrication approaches and performance characteristics. Xiao *et al*. developed CoCrFeNi-based HEA coatings via plasma spraying, revealing that CoCrFeNiMo and CoCrFeNiMn systems predominantly contained face-centered cubic (FCC) structures and oxides, with abrasion identified as the principal wear mechanism.[41] Gao *et al*. explored how plasma current influences the synthesis of CoCrFeNiMn HEA coatings using plasma transfer arc technology, revealing that a current of 65 A optimized microhardness and minimized wear, though friction coefficients exceeded those of ductile iron substrates.[42] Cold-sprayed FeCoNiCrMn and Al_2O_3-reinforced variants fabricated by Yin and Zou *et al*. exhibited lower wear rates compared to laser-clad counterparts, attributed to enhanced dislocation density and refined grain boundaries, with composite coatings achieving approximately 50% wear rate reduction.[43,44] Andrew and Xue *et al*. synthesized MnCoCrFeNi coatings through plasma spraying, with reported porosity of 7.4 ± 1.3% and Vickers hardness of 4.42 ± 0.60 GPa, demonstrating fatigue-dominated wear mechanisms.[45,46] Xiao *et al*. further produced atmospheric plasma-sprayed FeCoNiCrMn HEA coatings, where surface fluffiness arose from Mn volatilization/oxidation, while thermal annealing markedly improved both wear and scratch resistance.[47] Zhang investigated Sm_2O_3-modified FeCoNiCrMn composite coatings finding that Sm_2O_3 incorporation mitigated crack formation tendencies in HEA systems. Optimal Sm_2O_3 concentration (2%) yielded superior tribological performance, corrosion resistance, and minimal residual surface stress.[48]

To enhance the wear resistance of the grinding roller, FeCoNiCrMo and FeCoNiCrMn coatings were innovatively applied to its surface in this paper. Existing research on these two coating systems has primarily focused on investigating the impacts of fabrication processes, elemental composition, and dopant incorporation on their wear-resistant properties. Nevertheless, the influence of process parameters on the morphology, hardness, bonding strength, and porosity of the two coatings has been infrequently examined. Furthermore, comprehensive comparing their friction and wear behaviors under dry sliding friction conditions are notably lacking. Therefore, this paper presents the preparation of FeCoNiCrMo and FeCoNiCrMn high-entropy alloy coatings on the surface of white iron grinding rollers by plasma spraying technology. The study focuses on the effects of spraying current and spraying distance on the morphology, hardness, bonding strength, and porosity of the coatings, with particular emphasis on analyzing the tribological properties of both coatings.

2. Experiments

2.1 Coating preparation

In this experiment, white iron with dimensions of Φ25 mm × 10 mm (detailed composition in Table 1) was used as the substrate material. The coating materials, FeCoNiCrMo and FeCoNiCrMn high-entropy alloys, were produced through vacuum induction melting gas atomization (VIGA-100) using equimolar ratios (chemical compositions listed in Table 2). The surface of the base white iron was first polished with sandpaper and then cleaned thoroughly with absolute ethanol and acetone. After drying in an oven, the sprayed surface was sandblasted using brown corundum particles with a size of 0.526 mm. High-entropy alloy powder was then applied to the surface. Subsequently, the sample was cut into a semi-

cylindrical shape using a wire-cutting machine. The cross-sectional surface was polished with metallographic sandpapers of various mesh sizes. After polishing, any residual impurities and polishing agents were removed by ultrasonic cleaning. The coating was prepared by the LBP-100 plasma spraying equipment.

Referring to the literature, the parameters for the coating preparation process are as follows: spraying current of 600 A, spraying distance of 100 mm, main airflow rate of 50 L/min, and auxiliary airflow rate of 0.8 L/min. Additionally, to investigate the influence of process parameters on the cross-sectional morphology, hardness, bonding strength, and porosity of the coating, spraying current (I) and spraying distance (H) were selected as experimental factors (refer to Table 3). The fixed settings for the other spraying parameters were as follows: the powder feeding rate was set at 23 g/min.

2.2 Coating characterization and performance testing

Elemental distribution and microstructural features of the coatings were characterized using a Sigma 300 scanning electron microscope (SEM) coupled with an UltimMax 40 energy-dispersive spectroscopy (EDS) system. Porosity assessments were conducted via Image Pro-Plus 6.0 software, with five replicates per sample. Phase composition analysis was performed using a MINIFLEX600 X-ray diffractometer (XRD) operating at 5°–90° diffraction angles in continuous scanning mode. Surface chemical states and compositional profiles were evaluated through X-ray photoelectron spectroscopy (XPS) on a Thermo Scientific Nexsa platform. Microhardness measurements utilized an HV-1000SPTA Vickers hardness tester under a 9.8 N load applied for 10 s, with five distinct regions averaged for statistical reliability. Bonding strength was determined according to GB/T8642-2002 "Thermal Spraying—Determination of Tensile Bond Strength" using a DNS200 electronic universal testing machine, with results averaged across five trials. The test surface is a circular surface with a diameter of 25 mm. Tribological behavior was assessed on an MDW-02G high-speed reciprocating tribometer with a Si_3N_4 grinding ball (Φ6.35 mm) under dry reciprocating conditions: 15 N load, 2 Hz frequency, 10 mm stroke, and 20 min duration. Based on the test results of the roller surface temperature during the production and processing of grinding rollers, tests were conducted at 80 °C using a high-temperature module. Wear scar depth was quantified by the VR-3200 3D profilometer, while cross-sectional wear areas were derived through integral processing in Origin. Subsequently, coating wear rates were calculated using Eqs. (1) and (2).

$$V = S \times l \tag{1}$$

$$W = V/(FL) \tag{2}$$

where V denotes the volume of wear sustained by the coated sample (mm^3), S represents the cross-sectional area of the wear mark (mm^2), and l corresponds to the length of the wear trace (mm). W signifies the wear rate ($mm^3/(N \cdot m)$). Additionally, F signifies the force applied (in Newtons) to the opposing grinding ball, while L indicates the total distance over which sliding occurs (measured in meters).

The experimental flow is shown in Fig. 1.

Table 1: KmTBCr12 white iron chemical composition (wt%).

Substrate	C	Si	Mn	Cr	Mo	Ni	Cu	S	P	Fe
KmTBCr12	2.0~3.3	≤1.5	≤2.0	11~14	≤3.0	≤2.5	≤1.2	≤0.06	≤0.1	Bal

Table 2: High entropy alloy powder chemical composition (wt%).

Powder	Ni	Fe	Co	Cr	Mo	Mn
FeCoNiCrMo	20.8	18.69	20.04	16.78	23.69	...
FeCoNiCrMn	20.86	19.41	20.93	18.22	...	20.58

Table 3: Coating process parameters.

	Current/A	Distance/mm	Ar/L·min^{-1}	H_2/L·min^{-1}
Process parameters	550	80	50	0.8
	600	100		
	650	120		

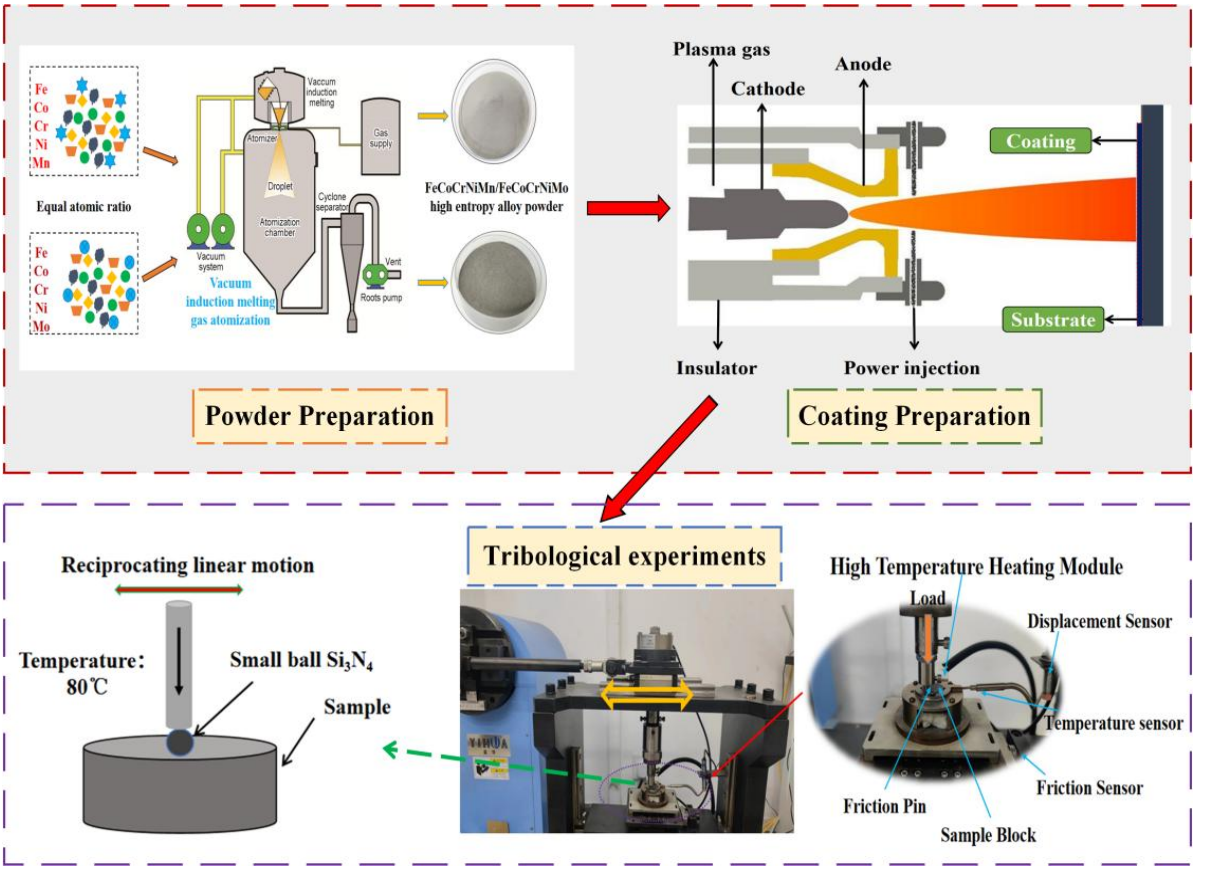

Fig. 1: Schematic diagram of experimental process.

3. Results and discussion

3.1 Phase and morphology of powder and coating

The microstructural characteristics and associated size distributions of VIGA-100 processed FeCoNiCrMo and FeCoNiCrMn high-entropy alloy particulates are presented in Fig. 2. As demonstrated in Fig. 2a and c, the majority of particulates exhibit near-spherical geometry with minimal irregular fragments observed. Quantitative analysis in Fig. 2b and d reveals distinct distribution patterns: FeCoNiCrMo displays characteristic diameters of D_{10}=25.50 μm, D_{50}=40.06 μm, and D_{90}=63.15 μm, while FeCoNiCrMn demonstrates finer particulates with D_{10}=13.37 μm, D_{50}=28.53 μm, and D_{90}=51.67 μm. Fig. 3 shows the SEM morphology and EDS element plane distribution of FeCoNiCrMo and FeCoNiCrMn powders, and various elements are evenly distributed on the powders. Compositional analysis indicates atomic percentages for FeCoNiCrMo as follows: Fe (20.93%), Co (21.27%), Ni (22.16%), Cr (20.19%), and Mo (15.45%). The FeCoNiCrMn contains constituent elements in these proportions: Fe (19.49%), Co (19.92%), Ni (19.93%), Cr (19.66%), and Mn (21.00%).

Fig. 4 shows the XRD patterns of two high-entropy alloy powders and coatings. Analysis of Fig. 4a reveals distinct phase compositions: FeCoNiCrMo particulates contain a FCC matrix coexisting with substantial σ-phase ($CrFe_{2.32}MoNi$), while the deposited coating exhibits dual FCC phases with enhanced oxide content.[8] The absence of σ-phase in coatings suggests thermal decomposition during plasma spraying, where elevated flame energies induce σ-phase oxidation into Fe-Cr oxides while facilitating alloying element dissolution. Mo incorporation induces lattice distortion in the primary FCC structure, leading to the formation of a modified FCC2 phase. This transformation correlates with oxidation processes producing $Fe^{2+}Cr_2O_4$ during deposition. As can be seen from Fig. 4b, both FeCoNiCrMn particulates and coatings maintain single-phase FCC configurations, with particulate diffraction peaks (43.57°, 50.76°, and 74.63°) corresponding to (111), (200), and (220) crystallographic planes.[49] Coating analysis identifies Mn-Cr-O spinel phases ($Mn_{1.5}Cr_{1.5}O_4$) without major structural transformations. Manganese addition promotes spinel formation while decreasing chromium solubility in the matrix, effectively suppressing potential FCC-to-BCC transitions.

The microstructural characteristics and elemental distribution patterns across coating cross-sections are illustrated in Fig. 5. Fig. 5a displays polished FeCoNiCrMo coating morphology with corresponding EDS maps, revealing five constituents homogeneously dispersed within the matrix. Chromium and iron demonstrate localized enrichment in darker regions, correlating with oxide formation. Comparative analysis of XRD data and SEM observations identifies light-toned zones as FCC matrix phases, while $Fe_{2+}Cr_2O_4$ compounds concentrate in darkened areas through elemental segregation. Fig. 5b exhibits analogous analytical results for

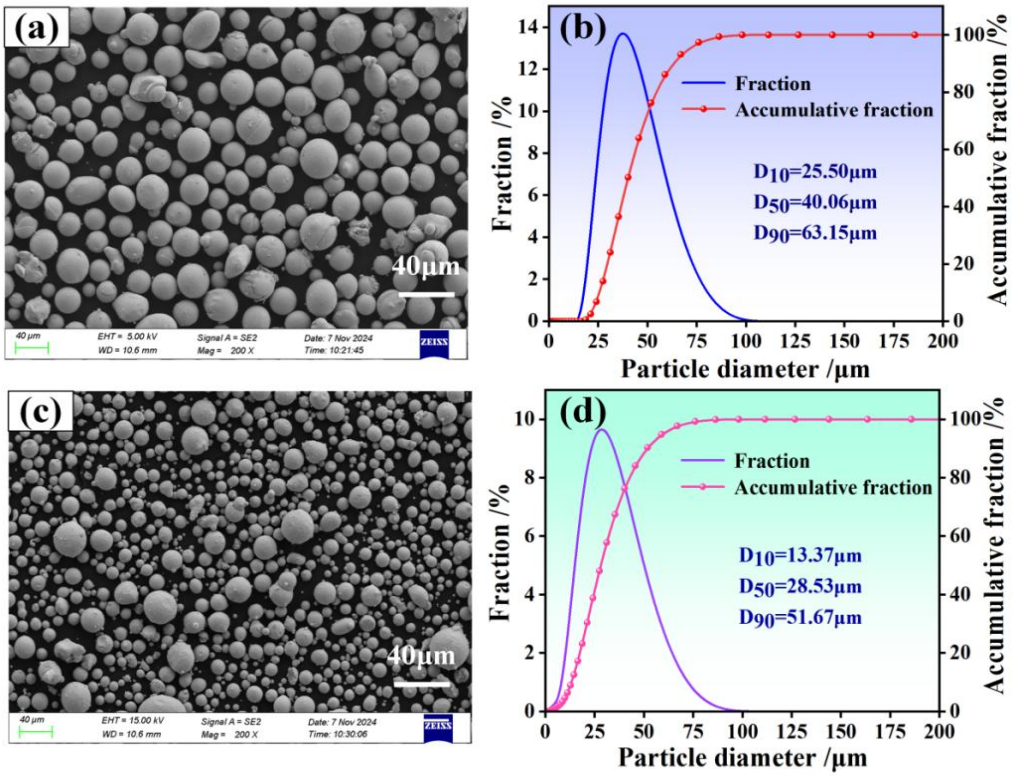

Fig. 2: Morphology and particle size distribution of FeCoNiCrMo (a, b) and FeCoNiCrMn (c, d) powders.

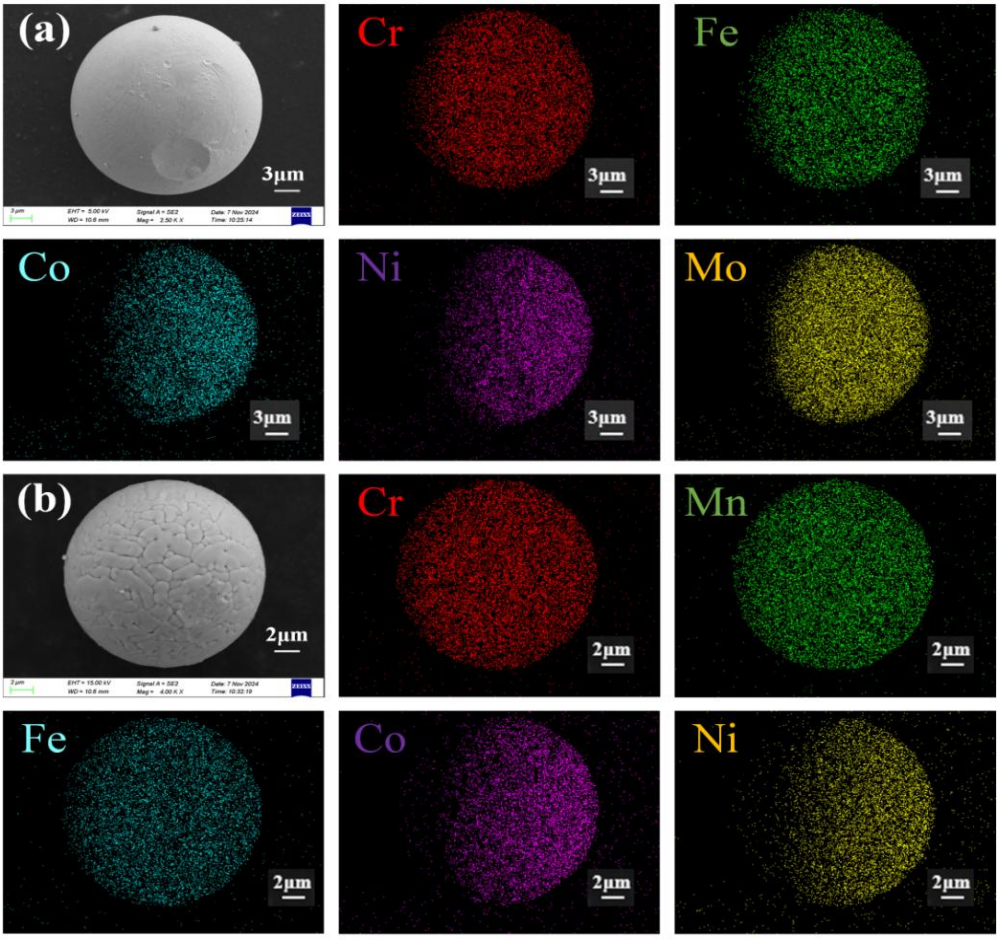

Fig. 3: SEM morphology and EDS element plane distribution of FeCoNiCrMo (a) and FeCoNiCrMn (b) powders.

FeCoNiCrMn coatings, where manganese and chromium exhibit similar partitioning behavior into oxide-rich domains. Alloy components maintain uniform distribution throughout the primary matrix structure. Phase identification through combined characterization methods confirms the light-gray matrix corresponds to FCC crystalline phases, with $Mn_{1.5}Cr_{1.5}O_4$ spinels preferentially forming in segregated regions.

3.2 XPS analysis of coating

The X-ray photoelectron spectroscopy profiles of HEA coatings and their high-resolution elemental spectra (Fe 2p, Co 2p, Ni 2p, Cr 2p, Mo 3d, Mn 2p) are displayed in Fig. 6. Spectral analysis reveals predominant oxide states for constituent elements, with minimal metallic presence observed - a consequence of plasma spraying's thermal effects enhancing elemental oxidation under atmospheric exposure. Table 4 details valence state distributions and corresponding binding energies for principal metallic components. Fe 2p analysis demonstrates FeO (709.35/722.46 eV; 709.66/722.63 eV) and Fe_2O_3 (711.53/724.53 eV; 711.48/724.55 eV) configurations in both coatings, respectively. Co 2p exhibits characteristic doublets for CoO (782.39/797.04 eV; 782.17/797.03 eV) and Co_2O_3 (779.99/795.33 eV; 780.19/795.22 eV), with triply-charged cobalt dominance suggesting preferential formation of Co_2O_3. This trivalent

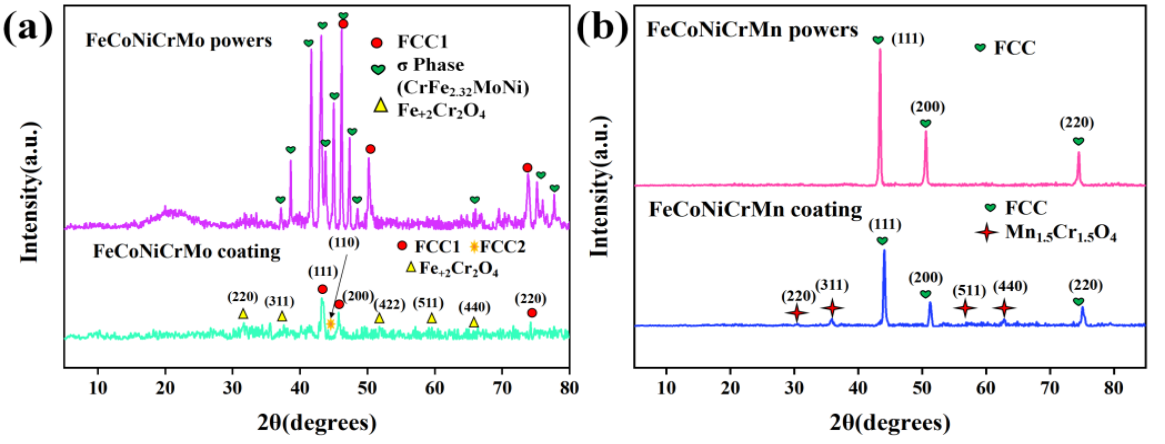

Fig. 4: XRD patterns of FeCoNiCrMo (a) and FeCoNiCrMn (b) high-entropy alloy powders and coatings.

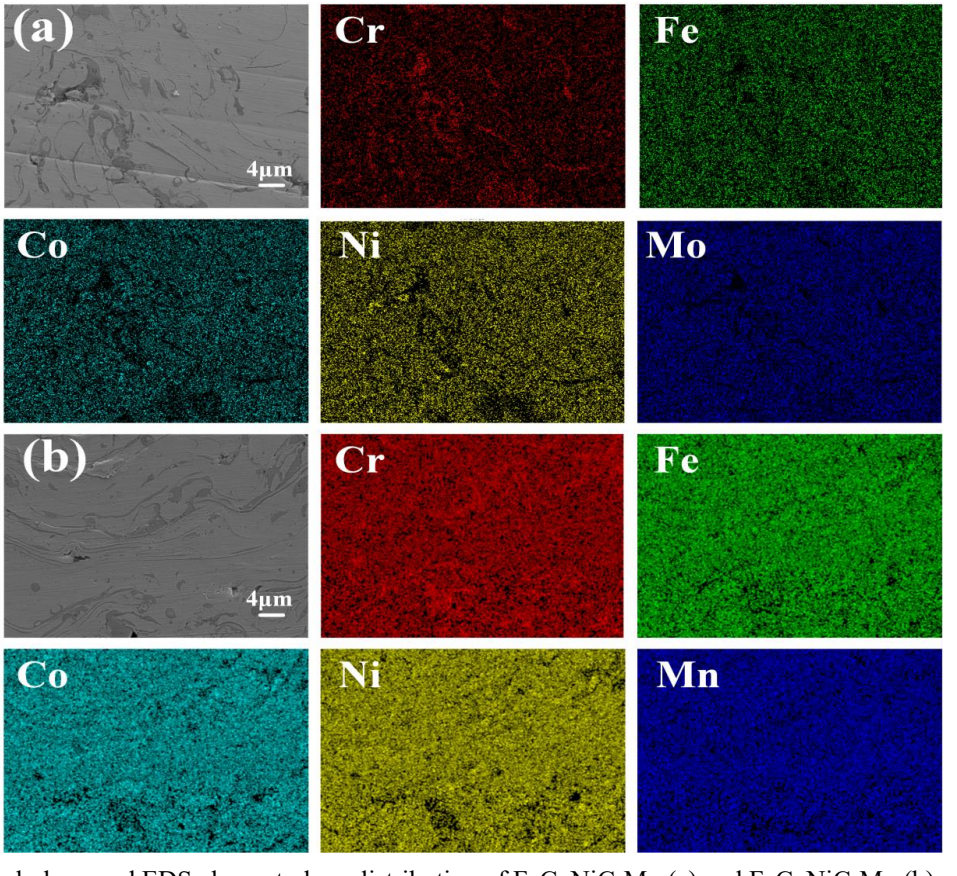

Fig. 5: SEM morphology and EDS element plane distribution of FeCoNiCrMo (a) and FeCoNiCrMn (b) coating sections.

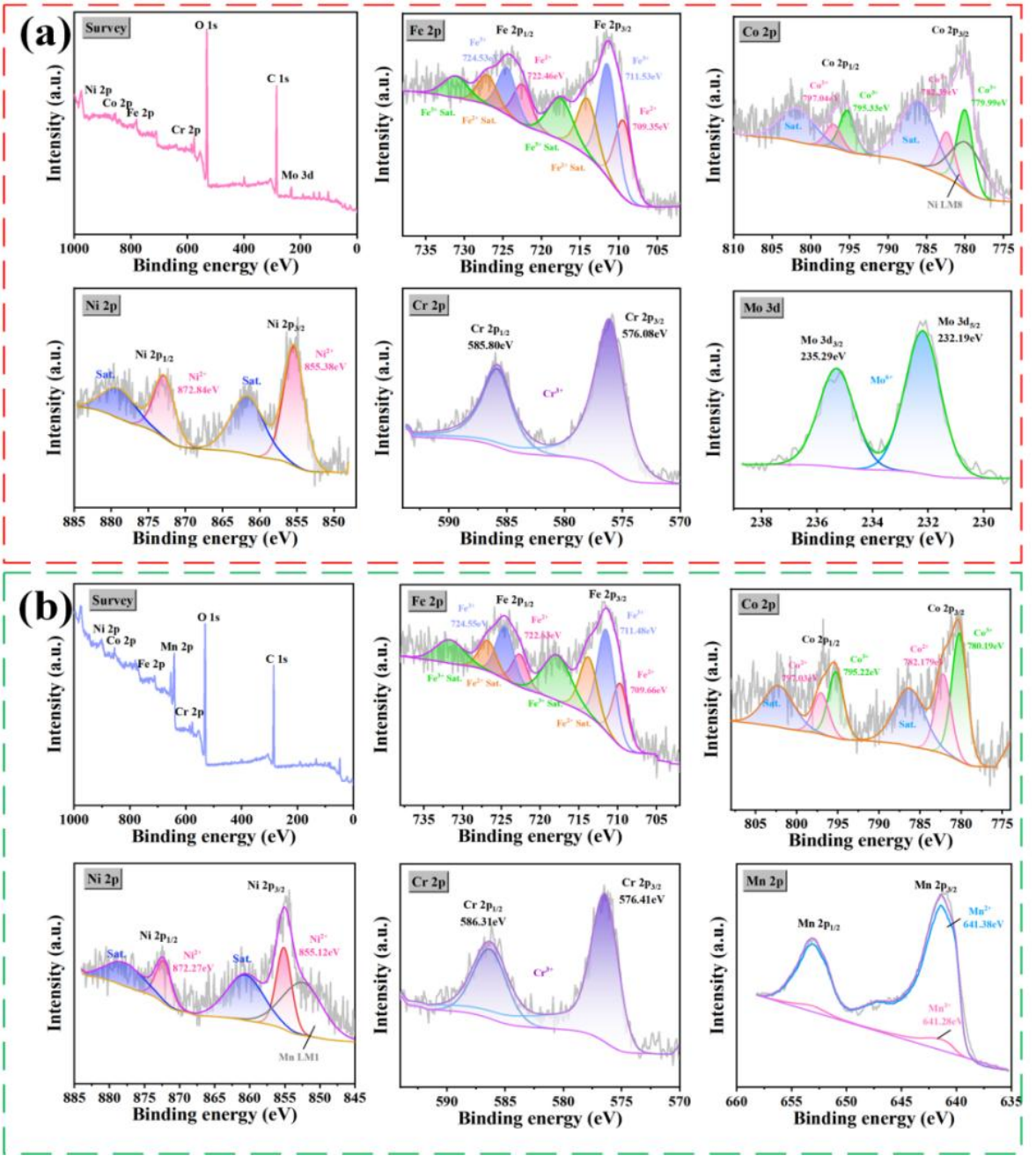

Fig. 6: XPS patterns of FeCoNiCrMo (a) and FeCoNiCrMn (b) coatings.

cobalt enrichment facilitates continuous oxide network development, potentially enhancing coating stability through protective oxide layer formation.

Ni 2p orbital spectral features exhibit characteristic NiO signatures (855.38/872.84 eV; 855.12/872.27 eV) accompanied by satellite peaks. Dominant peaks at 855.38/855.12 eV demonstrate nickel's primary oxide configuration, reflecting its superior oxidation resistance compared to iron and chromium which undergo preferential oxidation at oxide-metal interfaces. This nickel oxide formation confirms prior oxidation of Fe/Cr components. Cr 2p spectra reveal Cr^{3+} states through Cr_2O_3-associated peaks (576.08/585.80 eV; 576.41/586.31 eV), matching established chromium(III) oxide references (576.1/586 eV). The observed anhydrous Cr_2O_3 configuration, characterized by thermal stability and minimal structural defects, contributes significantly to coating densification mechanisms. Mo 3d analysis identifies dual oxidation states with Mo^{4+} (232.19 eV, MoO_2) and Mo^{6+} (235.29 eV, MoO_3) populations. Spectral intensity profiles suggest tetravalent molybdenum predominance, known for exceptional stability across pH environments. Hexavalent Mo species (MoO_3/MoO_4^{2-}) enhance chromium enrichment, facilitating optimized coating formation.[50] Mn 2p spectra display mixed Mn^{2+} (641.38 eV, MnO) and Mn^{3+} (641.28 eV, Mn_2O_3) states. Rapid oxygen diffusion kinetics in Mn/Cr systems drive selective oxidation during spraying, producing surface-enriched Mn-Cr oxide layers through preferential oxygen affinity.

Table 4: XPS analysis results of each element on the coating surface.

Type	Name	Start BE (eV)	Peak BE (eV)	End BE (eV)	Height CPS	FWHM (eV)	Atomic Ratio %
FeCoNiCrMo	Mo3d	240.41	231.99	228.91	3844.15	1.33	0.9
	C1s	291.11	284.8	279.61	35244.67	2.4	87.49
	Cr2p	594.41	576.41	572.11	5588.38	3.01	3.26
	Fe2p	740.41	710.93	704.71	4099.78	5.6	3.96
	Co2p	812.41	780.68	775.81	2819.53	4.16	2.28
	Ni2p	884.41	855.28	850.11	2968.67	3.35	2.11
FeCoNiCrMn	C1s	290.54	284.8	278.94	33916.93	2	77.71
	Cr2p	593.74	576.14	572.94	3820.94	2.47	2.17
	Mn2p	659.74	641.06	637.04	22463.98	3.41	12.85
	Fe2p	739.74	710.95	704.94	3587.91	4.93	3.33
	Co2p	811.74	780.24	775.74	2723.9	4.17	2.23
	Ni2p	883.74	854.68	849.74	2793.64	2.89	1.71

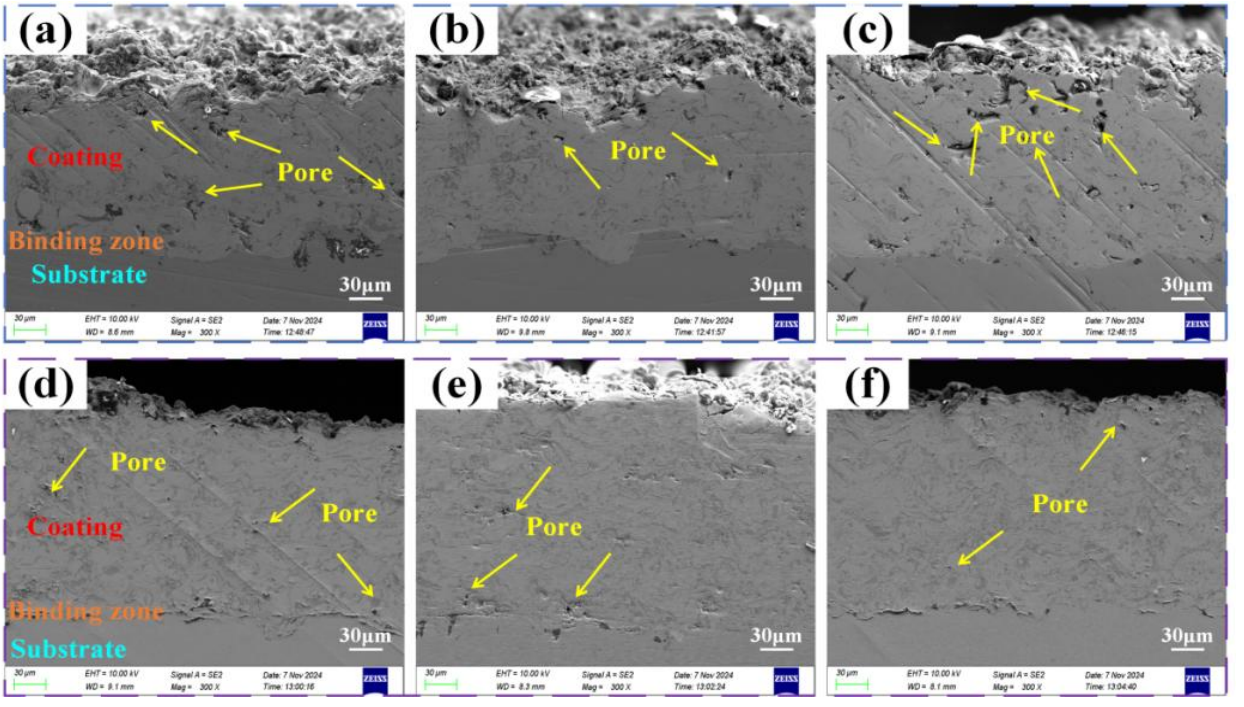

Fig. 7: Cross-sectional morphology of the coating under different spraying currents, FeCoNiCrMo: (a) 550 A, (b) 600 A, (c) 650 A; FeCoNiCrMn: (d) 550 A, (e) 600 A, (f) 650 A.

3.3 Effect of process parameters on microstructure and mechanical properties of coatings

Figs. 7 and 8 show the cross-sectional microstructural evolution of HEA coatings under different spraying currents and spraying distances. Metallurgically fused interfaces between the coating-substrate systems ensure robust adhesion.

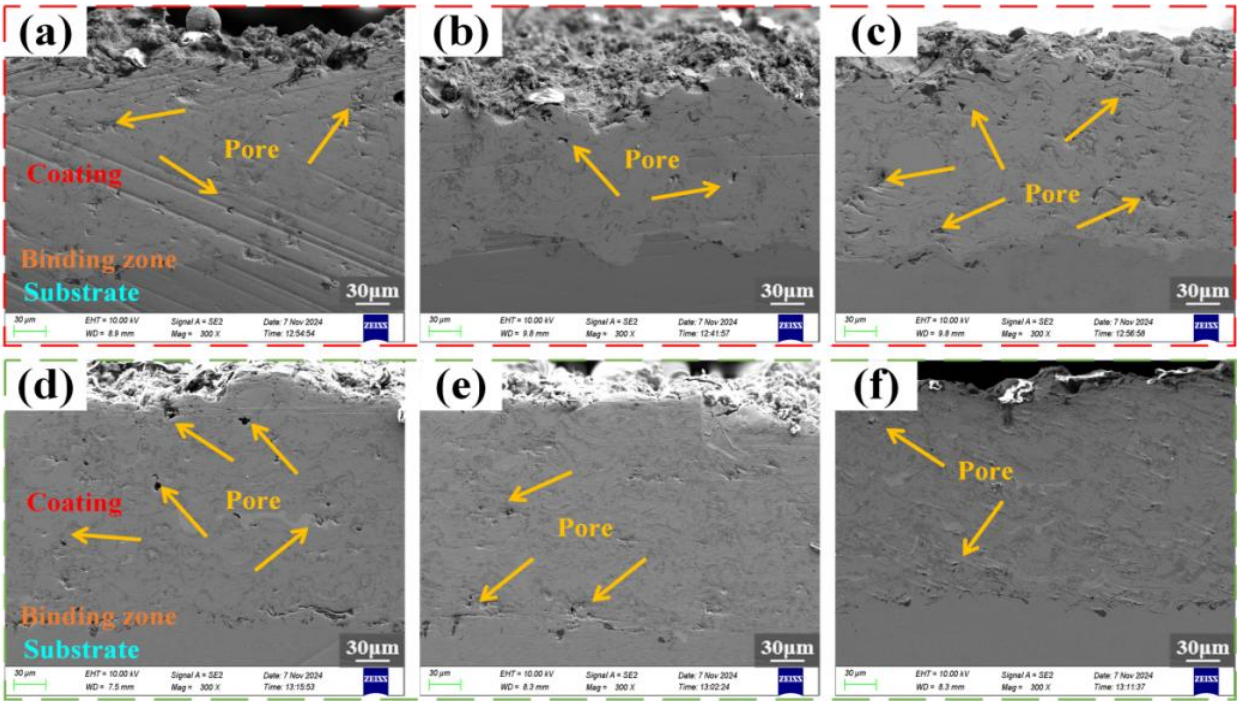

Fig. 8: Cross-sectional morphology of the coating at different spraying distances, FeCoNiCrMo: (a) 80 mm, (b) 100 mm, (c) 120 mm; FeCoNiCrMn: (d) 80 mm, (e) 100 mm, (f) 120 mm.

Fig. 7 demonstrates microstructural variations in the FeCoNiCrMo coatings fabricated at a fixed 100 mm spraying distance with current adjustments (550-650 A). When the spraying currents are 550 A and 650 A, the FeCoNiCrMo coating exhibits obvious holes and cracks; however, when the spraying current is 600 A, no obvious holes and cracks are observed. In contrast, as the spraying current increases, the holes in the FeCoNiCrMn coating gradually decrease, and at a spraying current of 650 A, no obvious holes or cracks appear. Fig. 8 illustrates cross-sectional microstructural variations in coatings deposited at fixed 600 A current with distances ranging 80-120 mm. FeCoNiCrMo coatings exhibit pronounced holes and cracks at extreme deposition ranges (80 and 120 mm) while maintaining structural integrity at intermediate 100 mm distances. Conversely, FeCoNiCrMn coatings demonstrate progressive defect density reduction with increasing standoff distance, achieving near-defect-free morphology at maximal 120 mm parameters.

Figs. 9a and b show the porosity of FeCoNiCrMo coating at different spraying currents and distances. It can be seen from the figure that the porosity of the coating decreases first and then increases under different spraying currents. At 600 A, it has the smallest porosity of 0.19%. This phenomenon correlates with plasma jet temperature elevation enhancing powder melting efficiency, thereby promoting uniform deposition. Excessive current intensification induces cumulative thermal stresses despite continued porosity decline, eventually generating microcracks through stress-driven defect propagation. Spraying distance optimization demonstrates analogous non-monotonic behavior, with minimum porosity (0.19%) observed at 100 mm. Particle dynamics analysis suggests two critical thresholds: insufficient acceleration below optimal distance reduces impact velocities, while supercritical distances enable particle deceleration. When the particle impact velocity is too low, the gas between the coatings cannot be discharged, and the holes and inclusions are easy to form, thus increasing the porosity of the coating. Contrastingly, FeCoNiCrMn coatings exhibit monotonic void reduction trends across identical parameters (Figs. 9c and d). Minimal porosity of 0.03% (650 A) and 0.04 % (120 mm) suggest operational parameters remained below critical thresholds required for void content reversal.

Fig. 10 demonstrates the variations in mechanical properties of two coatings with modified thermal spray parameters. Both hardness and bonding strength of FeCoNiCrMo coatings exhibit an initial enhancement followed by subsequent reduction across spraying current and spraying distance ranges. Maximum values of 530.3 HV and 40.6 MPa were achieved at 600 A current with 100 mm deposition distance. At shorter stand-off distances (80 mm), incomplete particle melting occurs due to reduced dwell time in the plasma jet, while limited acceleration duration restricts momentum acquisition, collectively diminishing impact forces on the substrate. Concurrently, excessive proximity induces oxygen entrapment within deposited layers, detrimentally affecting hardness. When exceeding 100 mm stand-off distance, particle velocity attenuation reduces interfacial deformation despite complete acceleration. The cohesive properties primarily depend on molten droplet characteristics optimal thermal states enhance flattening

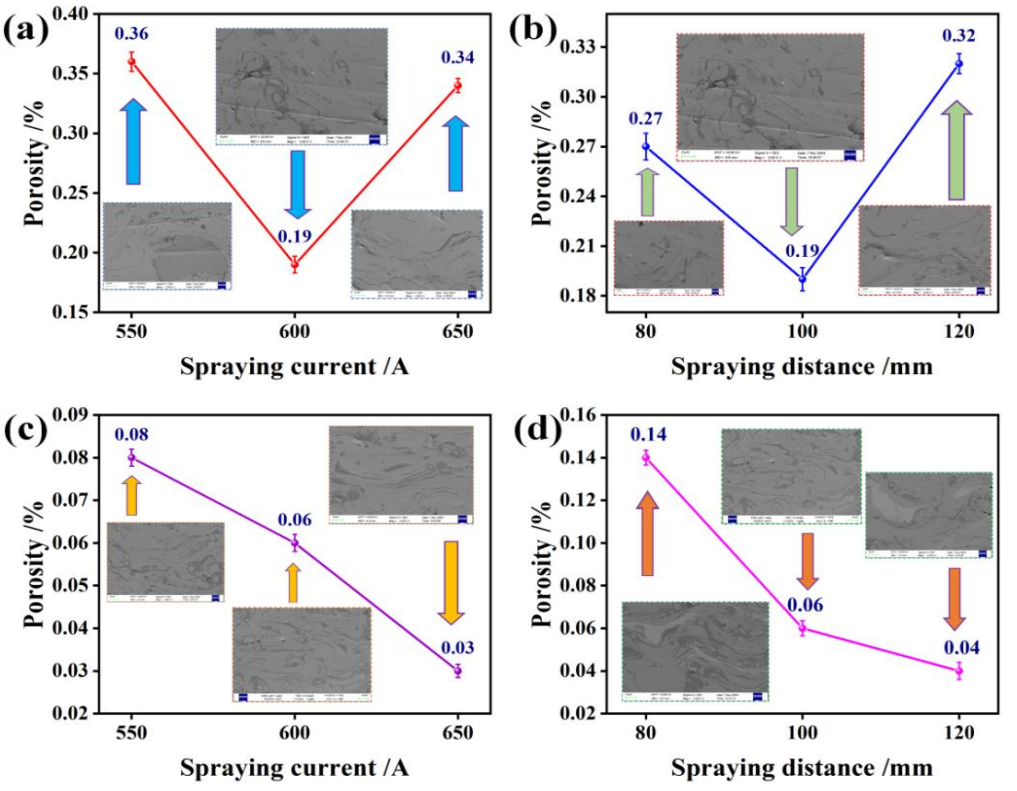

Fig. 9: Porosity of coatings at different spraying currents and distances, FeCoNiCrMo (a, b), FeCoNiCrMn (c, d).

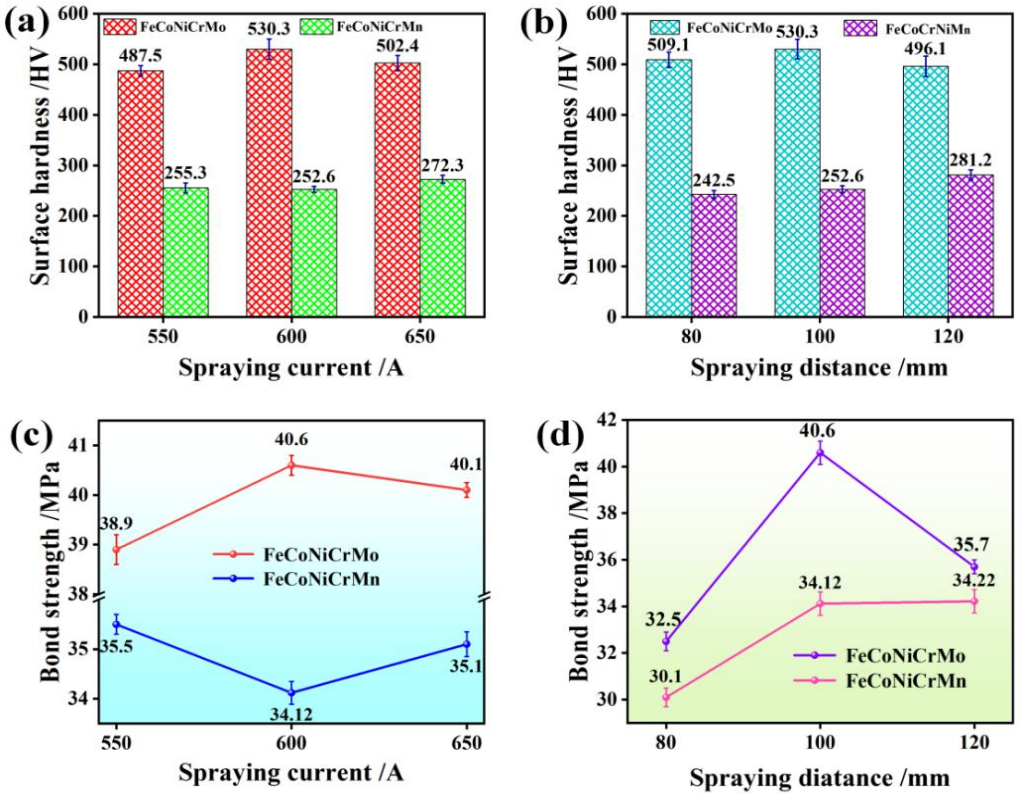

Fig. 10: Hardness (a, b) and bonding strength (c, d) of coatings under different spraying currents and distances.

behavior through improved wettability and sufficient kinetic energy transfer, promoting dense lamellar structures. Within the 550–650 A parameter window, increasing current initially improves particle melting efficiency; however, excessive energy input beyond critical thresholds abnormally elevates substrate temperatures. This thermal mismatch induces splashing phenomena, gas entrapment defects, and accelerated oxide formation through atmospheric interaction at elevated

temperatures, ultimately deteriorating interfacial integrity through crack propagation.[51]

The mechanical properties of FeCoNiCrMn coatings exhibit distinct variations under different deposition parameters. With increasing spray current, coating hardness and bonding strength initially decline before rising. This phenomenon occurs due to insufficient thermal input at 600 A, resulting in incomplete particle fusion. The presence of inadequately fused particulates and partially melted fragments compromises structural integrity, leading to reduced densification and diminished bond formation between deposited layers and substrate surfaces. Conversely, elevated spray distances result in continuous improvement in both mechanical characteristics. The observed performance enhancement correlates with operational parameters remaining below the critical thresholds required for optimal microstructural development during thermal spraying processes.[52]

3.4 Tribological properties of the coating

Fig.11 presents three-dimensional morphological features and cross-sectional profiles of wear traces observed on both substrate and coating surfaces. The analysis reveals lateral ridge-like formations adjacent to abrasion zones in all specimens, attributed to plastic deformation from accumulated debris during cyclic compression processes between Si_3N_4 spheres and test materials. Comparative measurements indicate distinct wear dimensions: the substrate exhibits 1.68 mm scar width with 0.12 mm maximum depth, FeCoNiCrMo coated specimen demonstrates 0.93 mm width and 0.023 mm depth, while FeCoNiCrMn surface shows intermediate values of 1.13 mm and 0.025 mm, respectively. Notably, the FeCoNiCrMo protected surface displays superior resistance to material degradation, evidenced by its minimal dimensional changes compared to other specimens.

Fig. 12 presents comparative data on tribological characteristics and surface morphology between the substrate and two deposited coatings. As shown in Fig. 12a, the bare substrate demonstrates relatively stable frictional behavior, whereas both coatings exhibit biphasic wear patterns corresponding to initial accommodation and subsequent stabilization phases. During the primary wear period, progressive escalation of frictional resistance occurs as interacting surfaces undergo geometric adaptation, followed by oscillatory behavior induced by debris generation within the contact zone. Quantitative analysis in Fig. 12b reveals

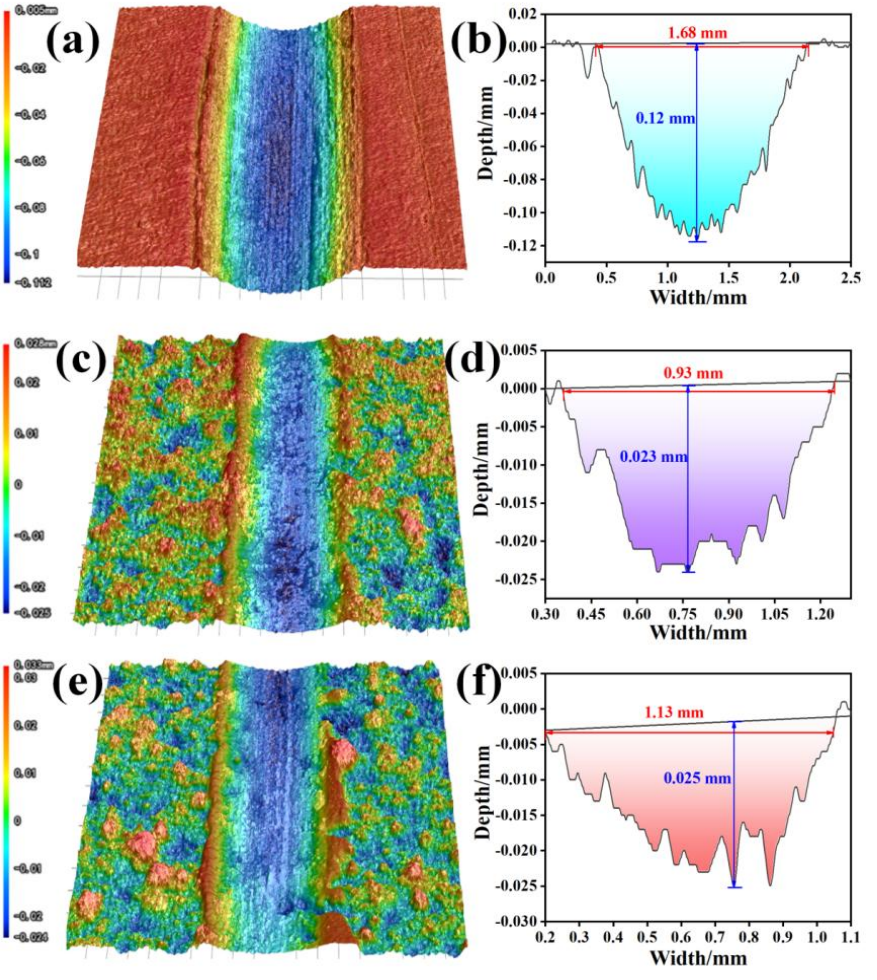

Fig. 11: Three-dimensional morphology and cross-sectional curve of wear scar: (a, b) Substrate; (c, d) FeCoNiCrMo Coatings; (e, f) FeCoNiCrMn Coating.

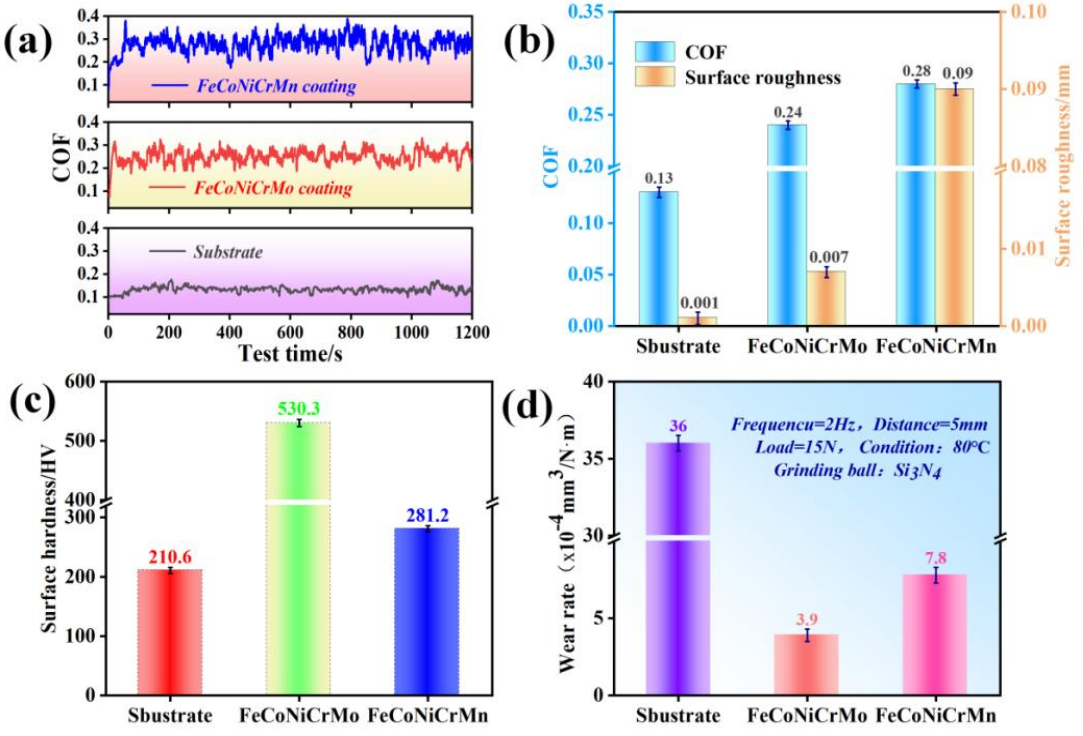

Fig. 12: Friction coefficient, roughness, hardness and wear rate of substrate and coating: (a) Friction coefficient curve; (b) Coefficient of friction and roughness; (c) hardness; (d) Wear rate.

distinct frictional parameters: 0.13 for the substrate, 0.24 for FeCoNiCrMo, and 0.28 for FeCoNiCrMn coatings, with corresponding surface texture measurements of 0.001 mm, 0.007 mm, and 0.009 mm. Compared to the base material, the two coatings exhibit a higher coefficient of friction and greater surface roughness. This increase in surface roughness enhances the actual contact area between the friction pairs and the shear force at the contact points, leading to an elevated coefficient of friction.[53-55]

The hardness and tribological performance of substrate and coating are quantitatively compared in Fig 12c and d. FeCoNiCrMo exhibits a microhardness value of 530.3 HV, representing a 152.8% enhancement over the substrate's 210.6 HV, while FeCoNiCrMn demonstrates 281.2 HV with 33.5% improvement. Corresponding wear rate measurements reveal significant reductions, with FeCoNiCrMo showing 3.9×10^{-4} mm³/(N·m) (89% decrease) and FeCoNiCrMn achieving 7.8×10^{-4} mm³/(N·m) (78% reduction) relative to the uncoated matrix. Microstructural characterization indicates that oxide phase distribution within deposited layers contributes to enhanced surface protection mechanisms through hardness elevation and adhesive wear mitigation, thereby optimizing wear resistance properties.[35]

3.5 Coating wear mechanism

The SEM images of the abrasive surfaces of the substrate and the coatings are presented in Fig. 13. As illustrated in Figs. 13 (a-c), the wear marks on the substrate are the widest, followed by the FeCoNiCrMn coating, and then the FeCoNiCrMo coating. This observation is consistent with the three-dimensional morphology depicted in Fig. 11. Figs. 13 (d-f) provide an enlarged view of the areas highlighted by the white boxes in Figs. 13 (a-c). As can be seen from Fig. 13d, there are blocky peeling and accumulation of grinding debris on the surface of the grinding marks of the substrate. Meanwhile, in combination with the scanning results in Table 5, Si and O elements were found in both the grinding debris accumulation (P2) and the furrow area (P1), indicating that the wear mechanism of the substrate is mainly adhesive wear, followed by slight abrasive wear. In addition, oxidation reactions also occur during the friction and wear process. As can be seen from Fig. 13e, there are obvious parallel furrows on the surface of the FeCoNiCrMo coating wear marks, which are formed due to the cutting and squeezing of the surface by Si_3N_4 small balls during friction. At the same time, there are cracks on the surface, which is because the coating has accumulated damage at the edge of the furrows during continuous friction and wear tests, promoting the formation and expansion of fatigue cracks. Figs. 14a and b show the elemental surface scanning results of the wear marks on the surface of the FeCoNiCrMo coating. The O element is mainly concentrated in the deep black area of the surface, while the Si element is relatively evenly distributed. At the same time, combined with P3 and P4 in Table 5, it can be seen that the content of O element is higher and the content of Mo element is lower in the dark black area, indicating that a more severe oxidation reaction occurred in the dark black area during the friction and wear process. Parallel furrows and cracks indicate that the wear mechanism of the FeCoNiCrMo coating is mainly abrasive wear, followed by fatigue wear. As can be seen from Fig. 13f, the wear mark

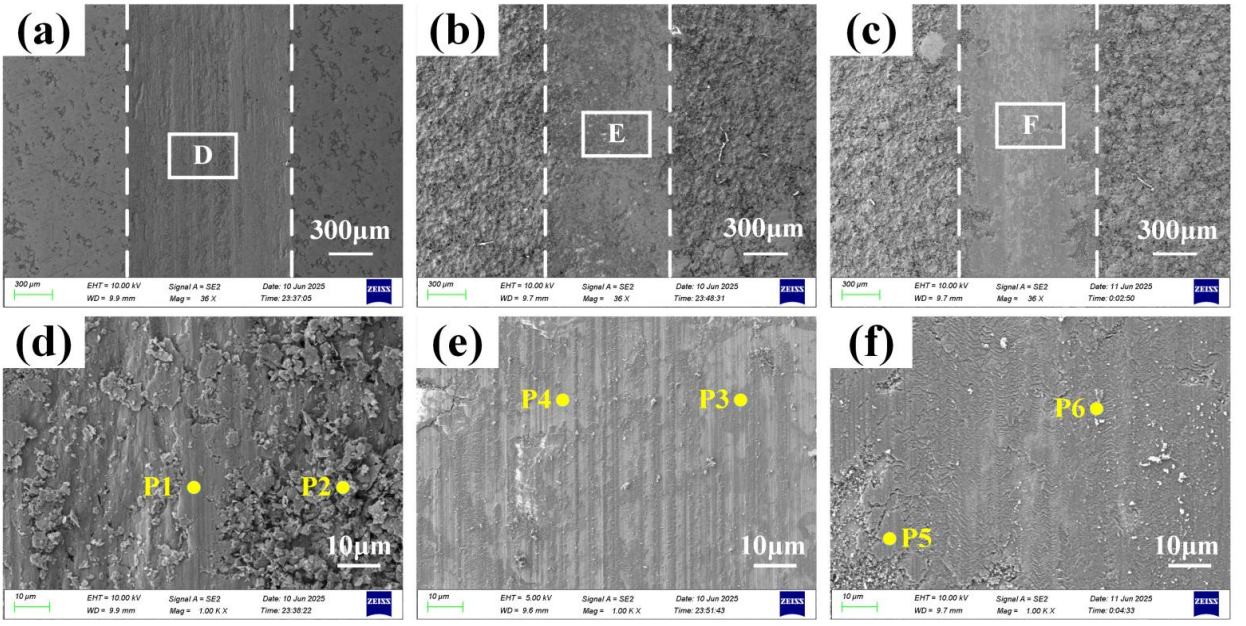

Fig. 13: SEM image of the surface morphology of the wear mark: (a) Substrate; (b) FeCoNiCrMo Coatings; (c) FeCoNiCrMn Coating; (d-f) enlarged views corresponding to the selected regions D in (a), E in (b), and F in (c), respectively.

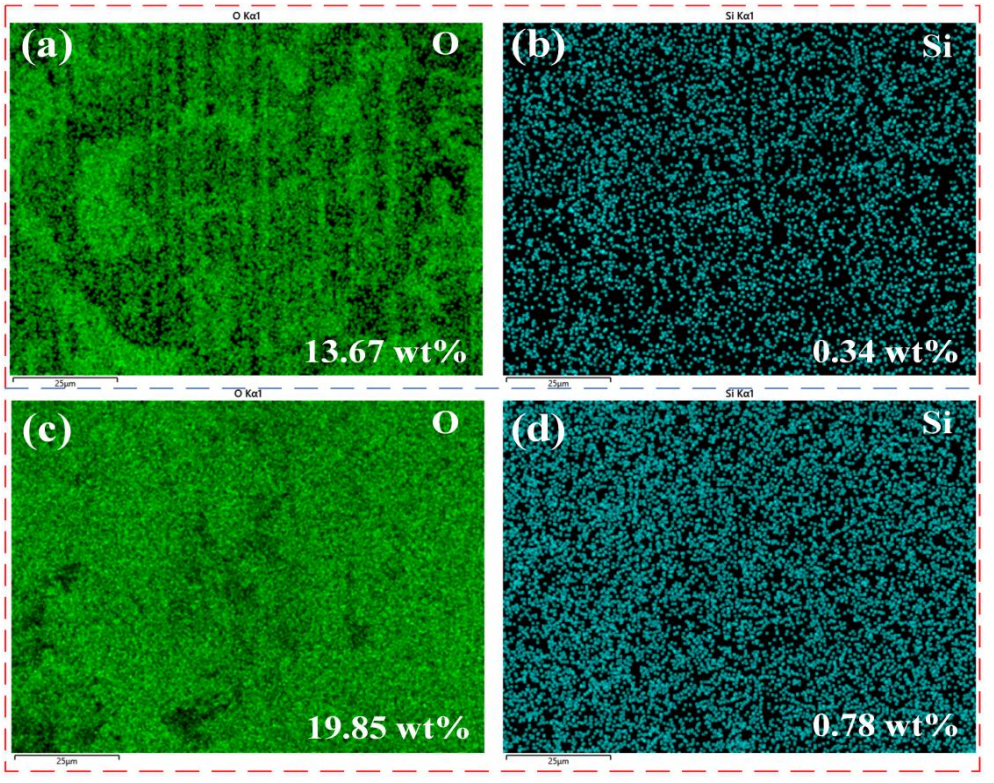

Fig. 14: The distribution and mass fraction of O and Si elements on the surfaces of the wear mark: (a, b) FeCoNiCrMo Coatings; (c, d) FeCoNiCrMn Coating.

surface of the FeCoNiCrMn coating has fatigue spalling holes and delamination spalling phenomena. According to the Si elements detected in P5 and P6 in Table 5, it indicates that the wear mechanism of the FeCoNiCrMn coating is mainly fatigue wear, followed by slight adhesive wear. Furthermore, in combination with Figs. 14c and d, it can be seen that the contents of O and si elements on the wear scar surface of the FeCoNiCrMn coating are both higher than those of the FeCoNiCrMo coating, indicating that it has undergone more severe oxidation reactions and adhesive wear during the friction and wear process.[56]

Fig. 15 shows the schematic diagrams of the wear mechanisms of two types of coatings. At the initial stage of friction, due to the presence of a large number of protruding

Table 5: P1-P6 EDS spot scan results.

Element/Wt%	P1	P2	P3	P4	P5	P6
C	5.61	4.22	7.68	5.86	1.17	1.72
O	1.36	3.91	22.05	19.06	21.61	21.49
Si	1.71	1.97	0.54	0.52	1.13	1.84
Cr	2.54	3.17	19.12	14.38	19.57	20.42
Mn	1.36	0.37	...	...		
Fe	85.80	84.46	13.08	13.11	17.04	16.55
Co	1.51	1.35	11.57	13.45	13.62	12.80
Ni	0.02	0.03	13.68	13.2	12.86	11.82
Mo	0.08	0.11	12.29	20.43	...	...

particles on the coating surface, as the friction and wear proceed, part of the abrasive particles are transformed into an oxide layer under the action of frictional heat. With the intensification of wear, microcracks appear on the wear track, and the generated abrasive debris will once again participate in the friction and wear process.[57,58] Due to its high hardness, the FeCoNiCrMo coating can better resist the cutting and ploughing effects of abrasive particles when subjected to external forces, thereby reducing material wear. Due to its low hardness, the FeCoNiCrMn coating generates more wear debris.

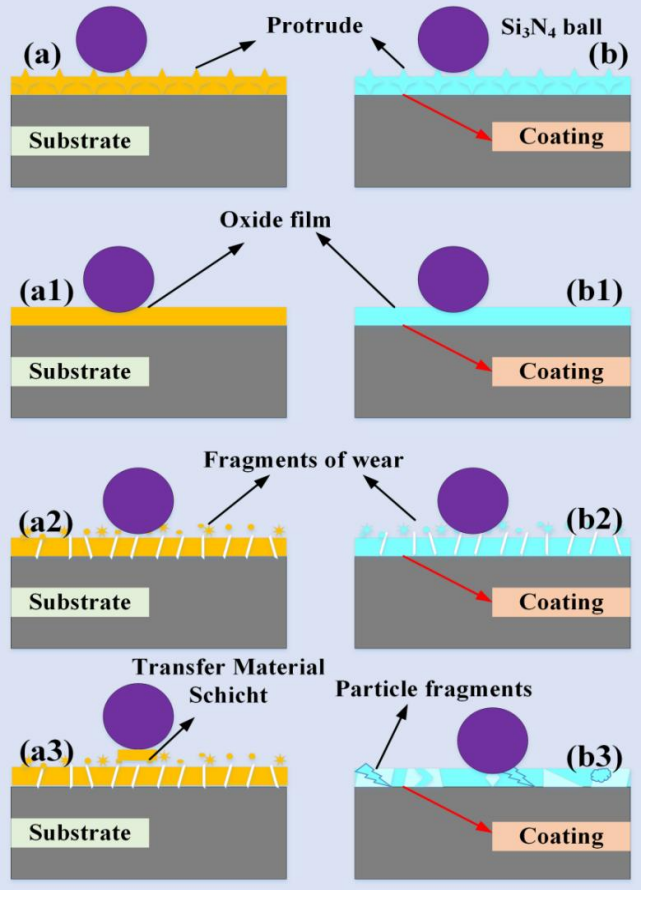

Fig. 15: FeCoNiCrMo (a, a1, a2, a3) and FeCoNiCrMn coating (b, b1, b2, b3) wear mechanism diagram.

4. Conclusion

FeCoNiCrMo and FeCoNiCrMn high-entropy alloy powders were used to produce coatings on KmTBCr12 white iron via plasma spraying. The effects of spraying current and distance on coating morphology, hardness, bonding strength, and porosity were examined, and the tribological performance of the coatings was compared. Both high-entropy alloy coatings have a multilayered structure achieved through metallurgical bonding. The FeCoNiCrMo coating comprises an FCC solid solution with $Fe_{+2}Cr_2O_4$ phases, while the FeCoNiCrMn coating consists of an FCC solid solution with $Mn_{1.5}Cr_{1.5}O_4$, and both exhibit a localized eutectic structure. The FeCoNiCrMo coating's porosity initially decreases then increases, while hardness and bonding strength first rise and then fall. At a fixed spraying distance, increasing the current reduces the FeCoNiCrMn coating's porosity, while hardness and bonding strength first decrease then rise. Furthermore, increasing the spraying distance decreases porosity and gradually improves both hardness and bonding strength. Under dry sliding conditions, the friction coefficients for the white iron substrate, FeCoNiCrMo coating, and FeCoNiCrMn coating are 0.13, 0.24, and 0.28, with wear rates of 36×10^{-4}, 3.9×10^{-4}, and 7.8×10^{-4} mm³/N·m, respectively. Compared to the substrate, the coatings reduce wear by 89% and 78%, and the wear mechanism shifts from adhesive wear to a combination of abrasive and fatigue wear.

Acknowledgments

This study was financially supported by the fund of Henan Key Laboratory of Superhard Abrasives and Grinding Equipment, Henan University of Technology (JDKFJJ2023003), the Key Research and Development Project of Henan Province (241111222100), National Natural Science Foundation of China (51775169), the Project of Zhengzhou Innovation and Entrepreneurship Team, the Joint Fund of Henan Science and Technology Research and Development Plan (242103810062), Research on Process Optimization and Adaptive Regulation of Environmental Behavior of Microporous Ceramic Materials for Grain Storage (24A460005).

Conflict of Interest

There is no conflict of interest.

Supporting Information

Not applicable.

References

[1] X. Wang, W. Wu, H. Jia, Research on wheat flour-making technology based on discrete elements, *Journal of Food Process Engineering*, 2023, **46**, e14446, doi: 10.1111/jfpe.14446.

[2] X. Wang, W. Wu, H. Jia, Calibration of discrete element parameters for simulating wheat crushing, *Food Science & Nutrition*, 2023, **11**, 7751-7764, doi: 10.1002/fsn3.3693.

[3] Y. Kunimitsu, The innovative use of modern materials, *Milling and Grain*, 2018, **129**, 56-58.

[4] S. Balasubramanian, K. Manonmani, Laser Heat Treatment of the Steel Bottom Rollers of Textile Machines Used for Producing Quality Yarns, *Lasers in Engineering*, 2015, **32**: 343-373.

[5] X. Cao, L. B. Shi, Z. B. Cai, Q. Y. Liu, Z. R. Zhou, W. J. Wang, Investigation on the microstructure and damage characteristics of wheel and rail materials subject to laser dispersed quenching, *Applied Surface Science*, 2018, **450**, 468-483, doi: 10.1016/j.apsusc.2018.04.210.

[6] M. Eloisa, The Ocrim revolution for cutting-edge matintenance, titanium rollers, *Milling and Grain*, 2019, **129**, 60-62.

[7] Y. Tian, J. Liu, M. Xue, D. Zhang, Y. Wang, K. Geng, Y. Dong, Y. Yang, Structure and corrosion behavior of FeCoCrNiMo high-entropy alloy coatings prepared by mechanical alloying and plasma spraying, *International Journal of Minerals, Metallurgy and Materials*, 2024, **31**, 2692-2705, doi: 10.1007/s12613-024-2902-z.

[8] Z. Liu, D. Kong, Microstructure, corrosive–wear and immersion corrosion performances of laser cladded FeCoNiCr–Mo (Al, Ti) high–entropy alloy coatings, *Corrosion Science*, 2024, **227**, 111766, doi: 10.1016/j.corsci.2023.111766.

[9] C. Cui, M. Wu, R. He, D. Jie, Y. Gong, X. Miao, Effect of LaB_6 doping on the microstructure, microhardness and corrosion behavior of laser cladded FeCoNiCrMo coating on Ti_6Al_4V, *Surface and Coatings Technology*, 2023, **466**, 129592, doi: 10.1016/j.surfcoat.2023.129592.

[10] L. Liu, J. Zhang, C. Zhai, H. Zheng, Addressing challenges in high-temperature oxidation of ultra-supercritical boiler tubes *via* FeCoNiCrMo high-entropy alloy coatings, *Surface and Coatings Technology*, 2024, **477**, 130351, doi: 10.1016/j.surfcoat.2023.130351.

[11] Y. Lu, Y. Peng, X. Chang, Z. Shi, Structural evolutions and tribological properties of laser cladded FeCoNiCrMo high-entropy alloy coating by laser remelting and tempering process: TEM and DFT calculations, *Tribology International*, 2024, **199**, 110000, doi: 10.1016/j.triboint.2024.110000.

[12] Q. Meng, Y. Li, X. Yu, W. Gong, Microstructure and properties of Al/FeCoNiCrMo coatings prepared by different plasma spraying currents on carbon fiber reinforced plastic surfaces, *Surface and Coatings Technology*, 2024, **494**, 131385, doi: 10.1016/j.surfcoat.2024.131385.

[13] N. Savage, Striking a balance with high-entropy alloys, *Nature*, 2021, **595**, S4-S5.

[14] Y. Yang, T. Chen, L. Tan, J. D. Poplawsky, K. An, Y. Wang, G. D. Samolyuk, K. Littrell, A. R. Lupini, A. Borisevich, E. P. George, Bifunctional nanoprecipitates strengthen and ductilize a medium-entropy alloy, *Nature*, 2021, **595**, 245-249, doi: 10.1038/s41586-021-03607-y.

[15] Z. Jiao, D. Hua, Q. Zhou, S. Li, D. Luo, H. Wang, W. Liu, Super-hard refractory high entropy alloy film with spinodal decomposition, *Journal of Materials Science & Technology*, 2025, **213**, 190-195, doi: 10.1016/j.jmst.2024.06.028.

[16] Y. Zhang, T. T. Zuo, Z. Tang, M. C. Gao, K. A. Dahmen, P. K. Liaw, Z. P. Lu, Microstructures and properties of high-entropy alloys, *Progress in Materials Science*, 2014, **61**, 1-93, doi: 10.1016/j.pmatsci.2013.10.001.

[17] M. Chuang, M. H. Tsai, W. Wang, S. Lin, J. W. Yeh, Microstructure and wear behavior of Al x $Co_{1.5}CrFeNi_{1.5}Ti$ y high-entropy alloys, *Acta Materialia*, 2011, **59**, 6308-6317, doi: 10.1016/j.actamat.2011.06.041.

[18] D. Hua, Q. Xia, J. Li, Q. Zhou, M. Xie, S. Liu, S. J. Eder, H. Wang, Atomistic insights into the role of graphene sheets in CoCrNi/graphene composites, *Acta Materialia*, 2025, **287**, 120809, doi: 10.1016/j.actamat.2025.120809.

[19] Q. Zhou, Y. Ma, M. Xie, Z. Ye, Z. Jiao, M. Yang, W. Ye, C. Yin, H. Teng, X. Lu, H. Wang, Fabrication and performance assessment of CoCrNi-based medium entropy alloy with silver-coated graphene, *Smart Materials in Manufacturing*, 2025, **3**, 100080, doi: 10.1016/j.smmf.2025.100080.

[20] Q. Ye, K. Feng, Z. Li, F. Lu, R. Li, J. Huang, Y. Wu, Microstructure and corrosion properties of CrMnFeCoNi high entropy alloy coating, *Applied Surface Science*, 2017, **396**, 1420-1426, doi: 10.1016/j.apsusc.2016.11.176.

[21] Z. Jiao, Y. Dong, Q. Li, Q. Zhou, S. Han, C. Yin, Z. Huang, X. Wang, H. Wang, W. Liu, Enhancing tribocorrosion resistance of VCoNi alloys in artificial seawater *via* nitrogen alloying, *Corrosion Science*, 2025, **243**, 112600, doi: 10.1016/j.corsci.2024.112600.

[22] O. N. Senkov, G. B. Wilks, J. M. Scott, D. B. Miracle, Mechanical properties of $Nb_{25}Mo_{25}Ta_{25}W25$ and $V_{20}Nb_{20}Mo_{20}Ta_{20}W20$ refractory high entropy alloys, *Intermetallics*, 2011, **19**, 698-706, doi: 10.1016/j.intermet.2011.01.004.

[23] B. E. MacDonald, Z. Fu, B. Zheng, W. Chen, Y. Lin, F. Chen, L. Zhang, J. Ivanisenko, Y. Zhou, H. Hahn, E. J. Lavernia, Recent progress in high entropy alloy research, *JOM*, 2017, **69**, 2024-2031, doi: 10.1007/s11837-017-2484-6.

[24] J. W. Yeh, S. Chang, Y. Hong, S. Chen, S. Lin, Anomalous decrease in X-ray diffraction intensities of Cu–Ni–Al–Co–Cr–Fe–Si alloy systems with multi-principal elements, *Materials Chemistry and Physics*, 2007, **103**, 41-46, doi: 10.1016/j.matchemphys.2007.01.003.

[25] A. Ahmad Siddiqui, A. K. Dubey, Recent trends in laser cladding and surface alloying, *Optics & Laser Technology*, 2021, **134**, 106619, doi: 10.1016/j.optlastec.2020.106619.

[26] H. Högberg, L. Tengdelius, M. Samuelsson, F. Eriksson, E. Broitman, J. Lu, J. Jensen, L. Hultman, Reactive sputtering of δ-ZrH_2 thin films by high power impulse magnetron sputtering and direct current magnetron sputtering, *Journal of Vacuum Science & Technology A*: *Vacuum*, *Surfaces*, *and Films*, 2014, **32**, 041510, doi: 10.1116/1.4882859.

[27] F. Zhang, X. Liu, G. Chen, W. Cheng, X. Li, J. Zhu, H. Zhao, Y. Zhang, G. Liu, Microstructure evolution and tribological properties of laser cladding Stellite6-Cu/Graphene composite coatings on TC4 alloy, *Tribology International*, 2025, **204**, 110463, doi: 10.1016/j.triboint.2024.110463.

[28] L. Wang, F. Zhang, S. He, Y. Luo, H. Jin, F. Yin, Plasma spraying *in situ* TiC reinforced AlCoCrFeNi composite coatings: Microstructure evolution and mechanical properties under post-annealing, *Materials Characterization*, 2024, **215**, 114168, doi: 10.1016/j.matchar.2024.114168.

[29] A. Meghwal, A. Anupam, C. Schulz, C. Hall, B. S. Murty, R. S. Kottada, R. Vijay, P. Munroe, C. C. Berndt, A. S. M. Ang, Tribological and corrosion performance of an atmospheric plasma sprayed $AlCoCr_{0.5}Ni$ high-entropy alloy coating, *Wear*, 2022, **506**, 204443, doi: 10.1016/j.wear.2022.204443.

[30] X. Qiu, Microstructure and mechanical properties of CoCrFeNiMo high-entropy alloy coatings, *Journal of Materials Research and Technology*, 2020, **9**, 5127-5133, doi: 10.1016/j.jmrt.2020.03.029.

[31] W. Zuo, W. Ren, Z. Fan, Y. Wang, Comparison of microstructure and properties of $FeCoNiCrMo_{0.2}$ and $FeCoNiCrMo_{0.5}$ high-entropy alloy coatings on the surface of $4Cr_5MoSiV$ steel by laser cladding, *Optics & Laser Technology*, 2025, **181**, 111877, doi: 10.1016/j.optlastec.2024.111877.

[32] T. Li, Y. Liu, B. Liu, W. Guo, L. Xu, Microstructure and wear behavior of $FeCoCrNiMo_{0.2}$ high entropy coatings prepared by air plasma spray and the high velocity oxy-fuel spray processes, *Coatings*, 2017, **7**, 151, doi: 10.3390/coatings7090151.

[33] Z. Wang, J. Zhu, Y. Guo, W. Xin, X. Hui, Y. Wu, H. Zheng, Y. Zhao, X. Wang, Multi-effects of Mo on enhancement of wear and corrosion resistances of FeCoNiCrMo x high entropy alloys coatings prepared by laser powder directed energy deposition, *Surface and Coatings Technology*, 2024, **477**, 130378, doi: 10.1016/j.surfcoat.2024.130378.

[34] H. Wu, S. Zhang, Z. Y. Wang, C. H. Zhang, H. T. Chen, J. Chen, New studies on wear and corrosion behavior of laser cladding $FeNiCoCrMo_x$ high entropy alloy coating: The role of Mo, *International Journal of Refractory Metals and Hard Materials*, 2022, **102**, 105721, doi: 10.1016/j.ijrmhm.2021.105721.

[35] Y. Fu, C. Huang, C. Du, J. Li, C. Dai, H. Luo, Z. Liu, X. Li, Evolution in microstructure, wear, corrosion, and tribocorrosion behavior of Mo-containing high-entropy alloy coatings fabricated by laser cladding, *Corrosion Science*, 2021, **191**, 109727, doi: 10.1016/j.corsci.2021.109727.

[36] C. Zhou, S. Wang, G. Wang, J. Zhang, W. Liu, Investigation on the microstructure, wear and corrosion resistance of $FeCoNiCrMo_x$ high-entropy alloy coatings deposited on 40Cr by laser cladding, *Journal of Materials Science*, 2022, **57**, 18615-18639, doi: 10.1007/s10853-022-07684-w.

[37] S. Zhang, W. Li, Y. Hu, T. Jiang, L. Guo, Y. Zhang, Y. Zhao, Effect of spraying power on the microstructure and wear behavior of the plasma-sprayed $FeCoCrNiMo_{0.2}$ coating, *AIP Advances*, 2021, **11**, 115110, doi: 10.1063/5.0074776.

[38] L. Wen, Q. Li, B. Yang, Z. Yang, J. Wang, P. Song, Oxidation behavior of FeCoNiCrMo high-entropy coatings by atmospheric plasma spraying on zircaloy-4 in steam at 1100 °C, *Crystals*, 2022, **12**, 1529, doi: 10.3390/cryst12111529.

[39] X. Ren, W. Sun, Z. Sheng, M. Liu, H. Hui, Y. Xiao, Effects of nano-CeO_2 on microstructure and properties of $WC/FeCoNiCrMo_{0.2}$ composite high entropy alloy coatings by laser cladding, *Nanomaterials*, 2023, **13**, 1104, doi: 10.3390/nano13061104.

[40] C. Cui, M. Wu, X. Miao, Z. Zhao, Y. Gong, Microstructure and corrosion behavior of CeO_2/FeCoNiCrMo high-entropy alloy coating prepared by laser cladding, *Journal of Alloys and Compounds*, 2022, **890**, 161826, doi: 10.1016/j.jallcom.2021.161826.

[41] J. Xiao, T. Li, Y. Wu, J. Chen, C. Zhang, Microstructure and tribological properties of plasma-sprayed CoCrFeNi-based high-entropy alloy coatings under dry and oil-lubricated sliding conditions, *Journal of Thermal Spray Technology*, 2021, **30**, 926-936, doi: 10.1007/s11666-021-01175-1.

[42] P. Gao, R. Fu, J. Liu, B. Chen, B. Zhang, D. Zhao, Z. Yang, Y. Guo, M. Liang, J. Li, W. Wang, Z. Yan, L. Zhang, Influence of plasma arc current on the friction and wear properties of CoCrFeNiMn high entropy alloy coatings prepared on CGI through plasma transfer arc cladding, *Coatings*, 2022, **12**, 633, doi: 10.3390/coatings12050633.

[43] S. Yin, W. Li, B. Song, X. Yan, M. Kuang, Y. Xu, K. Wen, R.

Lupoi, Deposition of FeCoNiCrMn high entropy alloy (HEA) coating *via* cold spraying, *Journal of Materials Science & Technology*, 2019, **35**, 1003-1007, doi: 10.1016/j.jmst.2018.12.015.

[44] Y. Zou, Z. Qiu, C. Huang, D. Zeng, R. Lupoi, N. Zhang, S. Yin, Microstructure and tribological properties of Al_2O_3 reinforced FeCoNiCrMn high entropy alloy composite coatings by cold spray, *Surface and Coatings Technology*, 2022, **434**, 128205, doi: 10.1016/j.surfcoat.2022.128205.

[45] A. S. M. Ang, C. C. Berndt, M. L. Sesso, A. Anupam, P. S, R. S. Kottada, B. S. Murty, Plasma-sprayed high entropy alloys: microstructure and properties of AlCoCrFeNi and MnCoCrFeNi, *Metallurgical and Materials Transactions A*, 2015, **46**, 791-800, doi: 10.1007/s11661-014-2644-z.

[46] M. Xue, X. Mao, Y. Lv, Y. Chi, Y. Yang, J. He, Y. Dong, Comparison of micro-nano FeCoNiCrAl and FeCoNiCrMn coatings prepared from mechanical alloyed high-entropy alloy powders, *Journal of Thermal Spray Technology*, 2021, **30**, 1666-1678, doi: 10.1007/s11666-021-01210-1.

[47] J. Xiao, H. Tan, Y. Wu, J. Chen, C. Zhang, Microstructure and wear behavior of FeCoNiCrMn high entropy alloy coating deposited by plasma spraying, *Surface and Coatings Technology*, 2020, **385**, 125430, doi: 10.1016/j.surfcoat.2020.125430.

[48] K. Zhang, W. Wang, W. Liu, C. Liu, J. Geng, H. Wang, H. Bian, Effect of Sm_2O_3 particles on microstructure and properties of FeCoNiCrMn composite coating by laser cladding, *Materials Chemistry and Physics*, 2024, **317**, 129168, doi: 10.1016/j.matchemphys.2024.129168.

[49] Z. Rong, C. Wang, Y. Wang, M. Dong, Y. You, J. Wang, H. Liu, J. Liu, Y. Wang, Z. Zhu, Microstructure and properties of FeCoNiCrX (XMn, Al) high-entropy alloy coatings, *Journal of Alloys and Compounds*, 2022, **921**, 166061, doi: 10.1016/j.jallcom.2022.166061.

[50] Y. Liang, M. Yang, D. Kong, T. Huang, J. Wang, Z. Yang, B. Zheng, P. Song, Effect of annealing on corrosion resistance and mechanical properties of Cr–Fe–Ni–Co–Mo–Si–B amorphous coating, *Journal of Materials Research and Technology*, 2024, **29**, 4622-4635, doi: 10.1016/j.jmrt.2024.02.104.

[51] J. Liang, K. Cheng, Y. Chen, S. Chiu, C. Chiu, J. Lee, S. Chen, Comparisons of plasma-sprayed and sputtering $Al_{0.5}CoCrFeNi_2$ high-entropy alloy coatings, *Surface and Coatings Technology*, 2020, **403**, 126411, doi: 10.1016/j.surfcoat.2020.126411.

[52] L. Tian, M. Fu, W. Xiong, Microstructural evolution of AlCoCrFeNiSi high-entropy alloy powder during mechanical alloying and its coating performance, *Materials*, 2018, **11**, 320, doi: 10.3390/ma11020320.

[53] X. Yu, Y. Sun, S. Wu, An analytical prediction of dynamic friction coefficient between rough surfaces considering adhesion forces, *Journal of Mechanical Science and Technology*, 2025, **39**, 2753-2766, doi: 10.1007/s12206-025-0435-7.

[54] A. Guinea, A. Aginagalde, W. Tato, I. Llavori, P. Garcia, L. Arraiago, A. Zabala, Impact of surface roughness on the coefficient of friction of polymer-on-polymer contacts for deflection pulley-rope systems in the lift industry, *Friction*, 2024, **12**, 2126-2138, doi: 10.1007/s40544-024-0881-8.

[55] S. Zhang, D. Li, Y. Liu, Friction behavior of rough surfaces on the basis of contact mechanics: a review and prospects, *Micromachines*, 2022, **13**, 1907, doi: 10.3390/mi13111907.

[56] S. Zhong, L. Chai, Z. Wang, T. Yang, Y. Liu, H. Dong, J. Shen, Y. Li, E. J. Cheng, X. Yin, H. Wang, Microstructures and tribological properties of laser-clad FeCrAl-TiX composite coatings on ferritic-martensitic steel, *Journal of Materials Research and Technology*, 2025, **36**, 922-938, doi: 10.1016/j.jmrt.2025.03.139.

[57] Y. Cao, K. Yan, W. Shi, R. Zhou, B. Li, J. Qin, Experimental study on the microstructure and tribological properties of laser-clad Ni60-WC composite coatings, *Materials*, 2024, **17**, 4638, doi: 10.3390/ma17184638.

[58] Q. Cao, L. Fan, H. Chen, Y. Hou, L. Dong, Z. Ni, Wear and corrosion mechanisms of Ni–WC coatings modified with different Y_2O_3 by laser cladding on AISI 4145H steel, *Science and Engineering of Composite Materials*, 2022, **29**, 364-377, doi: 10.1515/secm-2022-0163.